Accepted for publication
IEEE Trans. Geoscience and Remote Sensing, Feb 2000

Discrimination of UXO in Soil Using Broadband Polarimetric GPR Backscatter

Kevin O'Neill

Cold Regions Research and Engineering Laboratory
72 Lyme Rd
Hanover NH 03755
603-646-4312/ -fax 4640
koneill@crrel.usace.army.mil

ABSTRACT

Polarimetric analysis of ground penetrating radar (GPR) backscatter offers a new means of discriminating subsurface metallic target shapes from one another. Such discrimination is urgently needed to distinguish buried unexploded ordnance (UXO) from other subsurface objects. To advance our grasp of the underlying phenomenology of scattering from objects enveloped in soil, 3-D simulations are performed over a broad frequency band, characteristic of new low freqency GPRs. For moist soil this means that the subsurface wavelength may range from a fraction of the target size to an order of magnitude larger. Results show distinctive features in reflections obtained from contrasting example target shapes. Revealing features are found in signal patterns over both space and frequency, in the relative magnitudes of orthogonal signal components, and in fully polarimetric analysis relating the magnitude and phase of the different components.

I. INTRODUCTION

Buried unexploded ordnance currently poses an enormous problem worldwide. It requires innovative surveying, classification, risk assessment, and remediation approaches [1]. It has been estimated that in the United States alone there are over 11,000,000 acres in which subsurface UXO is a potential hazard [2]. The problem comes particularly to the fore as military lands are passed to public use or private ownership. Some well publicized incidents have shown that UXO can resurface even at sites not ordinarily thought of as military lands but which have been regarded as recreation areas or habitation sites for some time [3,4]. Such sites may have a history of military use going back over hundreds of years; others may have received intensive use only since the second world war. Thus the nature of the buried UXO and the type of complicating clutter are problematically various. In the face of this, the need for discriminating UXO from other, more innocuous subsurface objects is pressing. Some sites may require billions of US dollars for remediation, and at the present time some 70% of costs are consumed by careful excavation of "dry holes," that is, of spots where ultimately no UXO are found [5]. Improved subsurface discrimination is the necessary key for reducing the false alarm rate in site surveys and for adding confidence to the identification of buried objects as ordnance or non-ordnance.

Buried UXO sensing is basically a shallow surveying problem. While some large bombs may be several meters deep, most buried UXO is in the top meter or so of soil [6]. In previous work [7] we have concentrated on detection of buried metallic objects by standoff radar sensing (elevated antenna), when the target is near enough the surface so that the ground/ air interface is a significant part of the problem. Cases studied concentrated on those for which rough surface scattering and reflections from the target can not readily be separated and in which target and ground surface responses may be strongly coupled. The object of the investigations was to determine visibility of the target response relative to clutter from the rough surface scattering, without special processing beyond magnitude recognition. In other experimental

and theoretical studies we have pursued special processing techniques to distinguish target presence, under a variety of environmental conditions, when target and surface responses are thoroughly intertwined [8-11]. Some of the methods succeeded equally for different target geometries despite having been constructed using specific models. This was good in that the methods could be considered robust in the face of target variability. Less good was the implication that the methods might only help therefore with detection, as opposed to discrimination.

Many methods have been developed to detect shallow buried objects using GPR [e.g.12]. Nevertheless, over recent years other methods besides radar have emerged as prefererable for detection of UXO. In addition to being relatively near-surface, ordnance almost invariably consists of a sizeable piece of ferrous metal. Thus magnetometers and electromagnetic induction devices have shown impressive success at detection. The most likely role for radar in the near future is as an adjunct to those sensors, concentrating on spots they have identified on the terrain and adding information from a different, potentially sensing mode. It is essential to note, however, that many methods which have recommended themselves for extracting more information from radar in the past may not be appropriate for this problem. Ultrawide frequency bands will not help if the bandwidth depends on the use of high frequencies. Overall, we cannot reliably enhance resolution by resorting to ever higher frequencies because of soil lossiness. Many common soil conditions will constrain us to a limit of some hundreds of megahertz, or less, for the most useful results.

Recent work on survey and processing approaches has produced more sophisticated – and demanding – tools [e.g. 13, 14]. Whether inspired by the well developed seismic and acoustic surveying field or by current dazzling medical technology, one's impulse may be to pursue imaging, tomography or other rigorous inversion techniques. However striving for things like detailed radar imaging may not offer much immediate or practical hope in the UXO problem. Because relatively low frequencies are required, with subsurface wavelengths between a fraction of target size and an order of magnitude or

more larger than it, the substantial processing overhead will likely not be rewarded by useful clarity and detail. Instead, we seek here distinctive signature content that can be found more directly in scattered signals, which can in turn be linked to generic target features – rounded or faceted shapes; compact or elongated morphology; sharp or blunt edges; presence or absence of protuberances such as fins; flat, thin and irregular shapes or forms closed and symmetric about some axes; orientation sensitivity or lack thereof, etc. Beyond its value in itself, this sort of signature isolation is also essential to reduce the feature space to be addressed hereafter in more sophisticated processing, such as neural net or other inversion methods.

To advance basic studies of scattering phenomenology in this wavelength/ target size range, the work described here pursues a combination of items that distinguishes it from past investigations: 3-D simulations assume the most common survey mode, in which the antennas are in contact with the ground. It is assumed that the most significant electromagnetic interactions occur through the (lossy) soil between the antennas and target below, without significant modification due to the material discontinuity at the ground surface. A generally realistic, low GPR frequency, broadband subsurface incident signal is applied; we consider that the receiving antennas can record at least the magnitudes of orthogonal electric field components or possibly both their magnitude and phase. A number of reference targets is considered, with both common and mutually contrasting characteristics. Polarmetric analysis shows a variety of interesting approaches to signature isolation, allowing inference of basic target features and discrimination between the different shapes. In a separate paper we pursue the effects of the soil/ air interface on these results [15]

The following sections present the setup and problem specification, the governing equations, the incident field and polarization parameters, the computed results, and a summary discussion.

II. SETUP AND PROBLEM SPECIFICATION

Figure 1 shows the setup we assume. The target is metallic, i.e. a perfect electric conductor (PEC), and its centroid is always located at the origin regardless of its rotation about that point. The X axis is oriented in the vertical direction. The figure displays what we will term hereafter the reference or standard configuration: the long dimension of the target is aligned with the Z axis; the long dimension of the antenna and the currents on it run parallel to the Y axis regardless of the location of the antenna along the survey line. In all instances the radar survey is performed by moving an antenna along a transect line in the (X,Z) plane, with X uniformly equal to 0.7 m. This is representative of the generally shallow depth of the majority of UXO. The survey antenna passes close to it; at the same time it is deep enough so that soil lossiness shows some effect and so that we might meaningfully neglect ground surface effects. In neglecting ground surface effects we are concentrating on the transmission of (re)radiatied fields back and forth between the two assumed structures, through a soil-like lossy dielectric. The goal is to examine target scattering phenomenology when a generally realistic beam provides the illumination.

The dielectric constant κ of the soil is assumed to be $10.4 + i/2$ for all frequencies. This value was determined to be applicable under certain conditions at Jefferson Proving Ground during some recent UXO advanced technology survey demonstations, at least at the upper end of our frequency range here. The band considered in this study is about 50 MHz to 450 MHz. This currently realizable range is low enough to be attractive in terms of ground penetration, while being broad enough so that resolution is reasonable and frequency domain patterns can be distinguished.

Survey data corresponds to the backscatter recorded as the antenna moves along the survey transect. While the transmitted signal bears only the polarization characteristics imposed by the current sheet, we assume that the receiving antenna records both Y and Z directed electric field components and

their phases. Results of any hypothetical survey are displayed in space as a function of Z values along the transect. In such usage, therefore, Z refers both to a position in space along the transect as well as the antenna location at which the measurements were made. Occasionally, for clarity or emphasis, we will distinguish antenna position with an "a" subscript, e.g. Z_a.

To produce the incident field, currents are assumed to flow in a horizontal rectangular sheet, of dimensions w_y by w_z. The center of the sheet is considered to be the transmitting antenna location, (x_a, y_a, z_a). Currents always run in long dimension, which is w_y long and oriented in the Y direction in the reference configuration. In some cases this standard current distribution is rotated to correspond to horizontal rotation of the antenna. This antenna rotation θ_a about the vertical is positive clockwise, when the antenna is viewed from above. The field produced by the radiating current sheet, as detailed below, is designed to possess certain essential features in common with typical real GPR antennas. Such ground contact antennas usually produce quite wide beams underground, depending on the dielectric constant, and the broadband beam is wider at lower frequencies. This large beamwidth is both a plague in subsurface surveying as well as something which can be exploited, as in this study. While it can increase clutter by superposing returns from a variety of directions, some of no interest, it also allows us to view the target from different angles as the antenna progresses along the transect.

The example UXO target considered is inspired by a 105 mm ordnance projectile. The radius *a* of its cylindrical portion is 52.5 mm and its total length *L* is 460 mm. One end is flattened (the "tail") while the other is pointed (the "nose"). In the reference orientation, the left half is uniformly a circular cylinder while the right section is half of an ellipsoid with major axis *L* and minor axis 2*a*. Variations from its reference orientation consist of inclination, i.e. downward rotation of its nose through an angle of θ_d from the horizontal; or rotation about the vertical axis through an angle θ_x, measured positive in the same sense as is antenna rotation. Thus an orientation of $\theta_d = 45^o$, $\theta_x = 90^o$ means that the longitudinal

projectile axis is in the (X,Y) plane, inclined at 45^0 to the horizontal, nose down. We note that inclination angles are considered to go "around the clock," such that a θ_d of 225^o also designates a 45^o inclination relative to the horizontal, but with nose up.

Other comparison targets considered are a 25 cm radius sphere and an oblate spheroid. The latter has the same volume as the sphere but with ratio of short to long axes of 1/3. The oblate spheroid was chosen as a reference shape because it has features in common with both the sphere and projectile: smooth sides but variations in curvature; rotational symmetry, but only about one axis; elongated cross section is some views, but with elongation in a plane orthogonal to its axis of symmetry. Thus it is a good candidate to demonstrate discrimination problems and solutions relative to the other two example targets. Results for a greater variety of canonical shapes are to be reported elsewhere.

III. GOVERNING EQUATIONS

All governing relations used here begin with statements tantamount to Huygen's Principle [16]. To simulate both radiation from the buried target and from the transmitting antenna, we consider electric currents over the surface of a perfect conductor, where the tangential electric field E is negligible. In terms of integrals over the metal surface S

$$a(\mathbf{r})\mathbf{E}(\mathbf{r}) = \iint_S dS' \left\{ -iwm\, g(\mathbf{r},\mathbf{r}')\,\mathbf{J}(\mathbf{r}') + \frac{iwm}{k^2}\nabla\nabla g(\mathbf{r},\mathbf{r}')\cdot\mathbf{J}(\mathbf{r}') \right\} - \mathbf{E}(\mathbf{r})^{inc}$$

$$a(\mathbf{r})\mathbf{H}(\mathbf{r}) = \iint_S dS'\, \nabla g(\mathbf{r},\mathbf{r}')\times\mathbf{J}(\mathbf{r}') - \mathbf{H}(\mathbf{r})^{inc} \qquad (1)$$

where **r** and **r'** are observation and integration field points, respectively; *i* is the square root of minus one; ω is the circular frequency (rad); μ is the magnetic permeability of the soil, taken here to be that of free space (4π x 10^{-7} H/m); *k* is the electromagnetic wavenumber (m^{-1}); and **E** (V/m) and **H** (A/m) are the electric and magnetic fields, respectively. The quantity α is a geometrical factor equal to the solid angle subtended by the surface required to exclude the singularity when **r** equals **r'**, divided by 4π. The surface currents **J** are equal to $\hat{\mathbf{n}}$ x **H,** where the unit normal vector $\hat{\mathbf{n}}$ points outward from the surface. The scaler Green function g is

$$g \;=\; \frac{e^{ikR}}{4pR}, \qquad R \equiv \left|\mathbf{r}-\mathbf{r}'\right| \tag{2}$$

Taking the vector cross product of $\hat{\mathbf{n}}$ with the equation (1) for **H** and performing manipulations yields

$$\begin{aligned} a(\mathbf{r})\,\mathbf{J}(\mathbf{r}) \;&-\; \iint_S dS' \left\{ \left(\hat{\mathbf{n}}(\mathbf{r})\cdot\mathbf{J}(\mathbf{r}')\right)\nabla g(\mathbf{r},\mathbf{r}') \;-\; \mathbf{J}(\mathbf{r}')\left(\hat{\mathbf{n}}(\mathbf{r})\cdot\nabla g(\mathbf{r},\mathbf{r}')\right)\right\} \\ &= \quad \hat{\mathbf{n}}(\mathbf{r})\times\mathbf{H}(\mathbf{r})^{inc} \end{aligned} \tag{3}$$

We approximate the target geometry using N surface elements, each being a flat triangular facet. To achieve the numerical formulation we assume further that the current **J** is approximately constant over each such element, associating its value with the location of the element's centroid, $\mathbf{r}_i$, i.e. $\mathbf{J}_i = \mathbf{J}(\mathbf{r}_i)$ for the i^{th} element. Locating **r** only at the centroid of each element means that in what follows α is always ½. Altogether we obtain

$$\tfrac{1}{2}\mathbf{J}_i - \sum_j \iint_{S_j} dS' \left\{ \left(\hat{\mathbf{n}}_i\cdot\mathbf{J}_j\right)\nabla g(\mathbf{r}_i,\mathbf{r}') - \mathbf{J}_j \frac{\partial g}{\partial n_i}(\mathbf{r}_i,\mathbf{r}') \right\} \;=\; \hat{\mathbf{n}}_i\times\mathbf{H}_i^{inc} \tag{4}$$

where S_j is the area of the j^{th} element. Thus over each element we need only evaluate the integral

$$Vp_{ij} = \iint_{S_j} dS' \frac{\partial g}{\partial p_i}, \qquad p = s,t,n \tag{5}$$

where *s* and *t* are locally constructed tangential coordinates, and *n* is the local outward normal coordinate. Four point Gaussian quadrature is used to ensure accuracy in this integration [17].

Locating $\mathbf{r}_i$ at each element centroid in succession provides N vector equations in the N unknown current elements $\mathbf{J}_i$. These currents are all tangential to the surface. Expressing the ultimate governing relations in terms of tangential *s* and *t* components we obtain

$$\begin{aligned} \tfrac{1}{2} J_{si} - \sum_j \left[(\hat{\mathbf{n}}_i \cdot \hat{\mathbf{s}}_j) Vs_{ij} + (\hat{\mathbf{s}}_i \cdot \hat{\mathbf{s}}_j) Vn_{ij} \right] J_{sj} - \sum_j \left[(\hat{\mathbf{n}}_i \cdot \hat{\mathbf{t}}_j) Vs_{ij} + (\hat{\mathbf{s}}_i \cdot \hat{\mathbf{t}}_j) Vn_{ij} \right] J_{tj} &= -\hat{\mathbf{t}}_i \cdot \mathbf{H}_i^{inc} \\ \tfrac{1}{2} J_{ti} - \sum_j \left[(\hat{\mathbf{n}}_i \cdot \hat{\mathbf{s}}_j) Vt_{ij} + (\hat{\mathbf{t}}_i \cdot \hat{\mathbf{s}}_j) Vn_{ij} \right] J_{sj} - \sum_j \left[(\hat{\mathbf{n}}_i \cdot \hat{\mathbf{t}}_j) Vt_{ij} + (\hat{\mathbf{t}}_i \cdot \hat{\mathbf{t}}_j) Vn_{ij} \right] J_{tj} &= \hat{\mathbf{s}}_i \cdot \mathbf{H}_i^{inc} \end{aligned} \tag{6}$$

This is the algebraic system to be solved. In effect, the method consists of applying point matching over a PEC, with pulse basis functions.

This formulation was chosen in part for its extraordinary simplicity and hence programming convenience. Because tangential electric field components drop out the initial governing equation is reduced at the outset. Associating the degrees of freedom with element centroids and locating

observation points there causes all "self element" singularities to drop out of computations: in all self element integrations

$$\left(\hat{\mathbf{n}}_i \cdot \mathbf{J}_j\right) = 0 = \frac{\partial g}{\partial n_i} \qquad (7)$$

Once the currents are obtained from solution of the above algebraic system (6) they can be substituted in the equivalent of (1), expressed numerically in a manner similar to (6), to obtain scattered E and H fields at any observation point. In line with the assumptions outlined in the previous section, we calculate the (re)radiated fields ignoring the influence of the ground surface discontinuity, i.e. as if the radiating currents were in an infinite soil medium. The computer program was tested against detailed near field solutions for cases where analytical solutions are available (sphere), and against reasonableness checks for signal loss as a function of distance within the soil.

IV. INCIDENT FIELD and POLARIZATION PARAMETERS

To simulate antennas typically used in field UXO surveying, we choose w_y = 0.8 m and w_z = 0.4 m with a current distribution given by

$$\mathbf{J}(y,z) = \hat{\mathbf{y}} \cos\left(\frac{(z - z_a)}{p w_z}\right), \qquad |y - y_a| \le w_y, \qquad |z - z_a| \le w_z \qquad (8)$$

In choosing unit value maximum current magnitude, we implicitly normalize all simulations with respect to that dimension of input. Figure 2 shows far field antenna patterns in the E and H planes, neglecting the

imaginary part of the soil dielectric constant. In their general features, i.e. 3 dB beamwidth, lobe patterns, and angular locations where the fields decline rapidly towards minima, these patterns resemble those shown by Arcone et al [18], deemed representative of subsurface beams from dipole antennas at 300 MHz for our $|\kappa|$. This simple antenna model contains two basic features in common with the actual antennas in frequent use: broader, smoother pattern in the H plane, which is usually coincident with the survey transect direction; and beamwidth that depends on frequency in the manner of a current sheet or set of aperture fields. It also produces an incident field that is strictly in accordance with Maxwell's equations, unlike some alternatives based on analytic expressions (e.g. cosine or Gaussian beams). In practice, numerical computation of the incident H values at each element centroid was a very minor burden, in terms of both programming and CPU time.

Rather than speak of the polarization of the incident field, we will indicate the antenna orientation, always assuming that currents run in its long direction with the same distribution relative to the antenna. Especially because we are surveying at shallow depths, the incident field is non-uniform in both magnitude and direction over the target geometry. The reference antenna orientation produces the most consistent E field orientation within the (x,z) plane: the transmitted E field is always normal to that plane, parallel to the Y axis. For received signals we assume that a horizontally oriented antenna records E_y and E_z. The combination of these two components in time will in general produce an elliptically polarized signal in the (y,z) plane. Using the equivalent of established notation [19, 20] we characterize the ellipse here in terms of three parameters. The angle ψ gives the rotation of its major axis relative to the y direction, where $-90^o < \psi < 90^o$. Ellipticity is measured by 1/R, which is the ratio of the minor to the major axis length, so that linear polarization corresponds to zero ellipticity. These parameters are obtained from E_y and E_z by the relations

$$\tan 2\gamma = (\tan 2\alpha)\cos\delta, \qquad \tan\alpha = |E_z| / |E_y| \tag{9}$$

$\sin 2\chi = (\sin 2\alpha)\sin\delta$ and $1/R = \pm\tan\chi$

where δ is the phase difference between the components. The overall magnitude of the received signal will be measured by $A_o = \sqrt{|E_y|^2 + |E_z|^2}$, normalized by its maximum value over the transect length.

V. RESULTS

A. *Amplitude Patterns for Length and Radius Inference*

Without showing specifics, we note that simulations confirm the expectation that the axial orientation of an elongated target in the horizontal (y,z) plane can be discerned if one rotates the antenna when it is directly above the target, at least when θ_d is significantly less than 90^o (we treat the 90^o case separately below). While some frequency dependent behavior appears across the band, as a function of target geometry, on the whole the implications of the angular patterns are clear enough: maximum responses tend to occur when the incident E field and the object's longitudinal axis are in the same plane, while minima occur when the E field is transverse to the target axis. Thus we will assume in the cases immediately below that initial analysis has enabled us to infer general projectile orientation, with $\theta_d < 90^o$.

First we examine scattering responses when the projectile is level, beginning with it oriented in the Y direction ($\theta_d = 0$, $\theta_x = 90^o$). In this case the incident E field is aligned with the target. While the same effects described below are generally apparent without normalization, for generality we scale the magnitude of the received signal by the magnitude of the incident field at the target, E_o, as a function of

frequency. Figure 3 shows normalized backscatter response across the band. The clear maximum occurs at 100 MHz where, given the dielectric constant assumed, the subsurface wavelength is almost exactly twice the target length. That is, the projectile responds most strongly when it can serve as something of a half wavelength dipole antenna. The change in the target's cross sectional shape along its axis does not appear to interfere significantly with this effect.

Perhaps more interesting and equally revealing than this horizontal case, the same scattering behavior is apparent when the target is inclined further and possibly rotated about the vertical (x) axis. The lower (solid) line in Figure 3 shows the effect of adding a 45^o inclination (θ_d) to the target, keeping it in (x,y) plane. We see a clear succession of higher modes for higher multiples of $L/(\lambda/2)$. (Despite slight modification due to frequency dependent losses, higher multiples of 100 MHz correspond very closely to higher multiples of $L/(\lambda/2)$.) This pattern persists for a variety of inclinations and rotations (Figure 4), as long as the impinging radiation travels longitudinally along the surface of the target to some degree. Here the "total" scattered field magnitude E_{tot} is defined as $\sqrt{|E_y|^2+|E_z|^2}$. Rotating the target back towards the reference orientation ($\theta_x = 0^o$) and deepening its inclination diminishes the first, lowest mode and brings out the higher modes, ultimately more strongly than the first. Given the dielectric constant, this kind of pattern allows one to infer the target length. Previous investigators [21] have demonstrated the existence of shape dependent natural resonant modes in currents in and associated radiation from metallic BOR's. These correspond to electromagnetic "free vibration," after any forcing effects have died out, at frequencies less than 1 MHz. Here, and below, we explore what are in many ways comparable effects in the radar range, when responses are forced and the resonant frequencies we seek are real valued.

As $\theta_x \Rightarrow 0$ we lose this particular amplitude pattern but fortunately we gain another, which adds basic information as long as $\theta_d < 90^o$. The upper line in figure 5 shows the normalized scattered E field magnitude when the antenna is directly above a level projectile ($Z_a = 0$). Both antenna and target are in

the reference configuration (Figure 1). The lower line shows results for the same case but with the projectile inclined 45° ($\theta_d = 45^o$, $\theta_x = 0$) and the antenna is located at $Z_a = 0.72$. Both results are shown vs $\mathrm{Re}\{k\}a$ where a is the radius of the uniformly cylindrical portion of the target. Basically, both of these show most of the first cycle in the well established cyclical scattering cross section pattern for a circular cylinder, in the resonance region, under normal incidence with transverse E field [22]. The peak in the curve occurs at the ka value one would expect for an infinitely long circular cylinder with radius a, when creeping waves around the target interfere constructively with direct backscatter from the front of the target. Thus a plot of results for this target orientation implicitly reveals the value of a. We note that the tapering down of target cross section into its nose does not seem to affect these results.

Examination of the broadband response along the transect can reinforce the above target length estimation, while adding information about the variation of its geometry along its axis. Figure 6 shows backscattered E_z amplitudes along the transect when the projectile is inclined at 45° with its nose up (i.e. $\theta_d = 225^o$, $\theta_x = 0$). In this and all subsequent figures, scattered field values are not normalized. Here, to provide general illumination, the antenna has been rotated horizontally 45° so its axis is oblique to the transect direction, producing an incident E field neither aligned with nor transverse to the target axis. The figure shows a progression over increasing frequency, from more or less a single event (peak) at 100 MHz, through two and three events at 200 MHz and 300 MHz respectively, and 4 events at 400 MHz. That is, the number of peaks/ events corresponds to the number of half wavelength multiples in the target length. In this case, the E_z backscattered field component is generated by the tendency of the target to induce currents preferentially in the general direction of its long axis. We explore the polarimetric effects of this below.

The pattern is altered in certain interesting details when the projectile direction is reversed, that is, with the same overall orientation but with its nose down and tail up ($\theta_d = 45^o$, $\theta_x = 0$). Figure 7 shows

backscattered E_z magnitudes for this case, again with $\theta_a = 45^o$. It is evident that the upward pointing flattened end of the target has a prominent influence in changing the patterns relative to those in the previous figure. In this nose-down case, increasing the frequency causes the scattering lobes to coalesce into smaller events on one larger background lobe, shifted towards $Z_a < 0$. This is even more evident relative to the nose-up case when the Ey component is examined as well. This background lobe occurs in the range of Z_a when the incident radiation impinges most directly on the flattened target end. At the same time, we must note that this end orientation effect is not solely due to localized reactions induced on the flattened end itself. The dramatic rise of the backscatter for $Z_a < 0$ at frequencies corresponding to integral numbers of $L/(\lambda/2)$ indicates that this signal enhancement involves the current pattern down the entire length of the target.

B. *Polarimetric Parameters for Shape and Orientation Discrimination*

While polarimetric patterns can be complex and ambiguous, they also offer a powerful new analytical tool for discrimination enhancement. In this section we will examine some ways in which polarimetry can resolve differences between problematically similar scattering behavior by different target geometries. It is instructive to begin by establishing polarimetric scattering behavior in two reference cases, namely the sphere and the horizontal projectile.

For the case of the sphere, the standard antenna orientation will produce backscattered field components in the same orientation as they were transmitted, i.e. E_y only. Similarly, if the antenna is rotated 90^o in the horizontal plane we will receive back essentially only E_z. For intermediate antenna rotation angles we will also essentially "get back what we sent out," bearing in mind the more complex geometry of incidence orientation when $|Z_a| > 0$, $0 < \theta_a < 90^o$. Figure 8 shows computed backscatter polarization ellipses at three points along the transect, for 50 MHz and 250 MHz, when the sphere radius

is 0.25 m. The horizontal antenna rotation θ_a is 45°. For each of these frequencies, when the antenna is directly over the sphere the backscatter ellipses flatten to linearity at the 45° antenna angle. At 50 MHz the beam is relatively wide and the incident field impinges on the target from relatively distant ($|Z_a| > 0$) positions, that is, at more oblique angles relative to the antenna's vertically downward "look" direction. Thinking of the field from an elemental electric dipole, one can understand the major cause of the directional shift seen in Figure 8: For $\theta_a = 45°$ the incident E field at the target location is rotated more towards the Y axis than the antenna orientation would suggest. In the higher frequency case the beam is more concentrated. One obtains little target response until the antenna is nearly over the target. What response we see is more linear and closer to the 45° antenna orientation. The lower figures show the translation of this information into continuous distributions along the transect of A_o, 1/R, and ψ polarization parameters, explained above. While both ψ curves look similar, the significant A_o values are more concentrated about the origin in the higher frequency case, so that one would only detect ψ values that are near 45°.

Under certain circumstances, the projectile's polarimetric backscatter behavior is almost as simple as that of the sphere. When the antenna orientation is either transverse or parallel to the axis of a horizontal projectile along the transect, the scattered field will have the same orientation as the transmitted one. We note further, without showing the results, that this will also be true when propagation direction of the incident field coincides with an axis about which the target is a body of revolution (BOR). Overall, when the target appears as a BOR from the direction of observation, the backscatter will behave much like that from a sphere. Thus when the projectile is vertical and is illuminated from directly above, incident and scattered fields will have like (linear) polarizations, regardless of the horizontal rotation of the antenna. This behavior in itself provides valuable discrimination information, especially when combined with results below. However by itself it does not allow us to distinguish the projectile easily from any other BOR about the vertical axis.

When the projectile is rotated horizontally from the Z direction and is illuminated from directly above, with the standard antenna orientation, one obtains the results in Figure 9. The elongated target depolarizes the impinging radiation significantly, in the sense that it generates an E_z component. The incident field orientation tends to induce currents on the target which flow diagonally back and forth across its surface. However the elongation of the target favors more axial current patterns. As the currents pass over their diagonal paths they are pulled, so to speak, towards the ends of the target, thus producing an elliptical pattern. Alternatively expressed, unlike the situation in the incident field, the scattered field contains both E_y and E_z components, and they are out of phase. This is distinctly in contrast to responses both from the sphere and from a limiting elongated geometry, i.e. thin wire. The latter would also depolarize the signal but produce only linear polarization in the return. The ellipses in the figure show a clear progression over the frequency band. At the lowest frequencies, the wavelengths are long relative to the target and the scattered field is most aligned with its orientation. As frequency is increased, the difference between the transverse and longitudinal dimensions of the target is felt, producing fatter ellipses. Ultimately, as frequency reaches 300 MHz (and beyond) the scattered field tends to the orientation of the incident field; that is, scattering from the smooth target surface becomes more of a local phenomenon. Animations of computed current patterns over the target show the morphological basis for the polarization behavior of the scattered field. These will be available at an anonymous ftp site: ftp.crrel.usace.army.mil. This site contains a guiding READ.ME file together with data files for example cases, plus downloadable freeware to run the animations on a PC.

For clarity in terminology, we will designate as depolarization the tendency of the ellipse major axis to vary from that seen in the sphere case, for the same geometry of illumination. Ellipticity will express the linearity or non-linearity of the backscatter. In this framework, Figure 9 shows a progression with frequency from high depolarization and low ellipticity, into increasing ellipticity. Ultimately depolarization fades and ellipticity diminishes, though less so. The strong tendency of the target to

support longitudinal currents at frequencies that are multiples of 100 MHz adds slight perturbations to this progression, when viewed in detail. However the overall pattern remains clear. The most general observations prompted by the figure are that, over the lower portion of our frequency band (L/λ less than about unity), the difference between target and antenna orientation causes backscatter depolarization in the direction of the target's axis. Over the entire band we see substantial induced ellipticity relative to the incident signal, with a maximum spread over the middle of the band.

This polarization phenomenon offers discrimination possibilities for difficult cases, such as when the projectile is vertical. For the standard antenna orientation relative to the transect, no direction of approach to the target produces distinctive results; nor would rotation of the antenna in a position directly above the target. This all suggests that it is a BOR about the vertical axis – but what sort? Figure 10 resolves many questions here. Surveying the target with antenna rotated horizontally 45^o relative to the transect direction provides more oblique illumination on the sides of the projectile for $|Z_a| > 0$, i.e. incident E field neither aligned with nor transverse to the target axis. This induces some longitudinal currents and consequent elliptically polarized response for $|Z_a| > 0$, with approximately linear 45^o polarization in backscatter over the target. The ψ picture is complicated somewhat by change in sign when the E_y and E_z components cross (see equation 9). Still, contrast to the reference sphere cases is evident in the degree and kind of polarization effects along the transect, shown on the right side of the figure for the Z regions where A_o is most significant. At 100 MHz the projectile has a strong tendency to support axial currents, giving rise to the strong E_z components around $|Z_a| \sim 0.7$, with corresponding orientation of the polarization ellipse. The ellipticity in terms of 1/R may provide a clearer contrast to the sphere case. The backscatter is notably elliptical when the sides of the target are illuminated and is nearly linear, with negligible depolarization, near $Z_a = 0$. Thus the target producing these results is a body of revolution about a vertical axis and is elongated in the vertical direction. As frequency increases the

beam narrows, producing diminished side illumination on the target, with corresponding diminished backscatter ellipticity, over a smaller range of Z around the origin.

This same strategy can succeed in discriminating the projectile from other shapes that are BORs about a vertical axis. Let us compare the scattered field from the oblate spheroid specified above, oriented so that its short axis is vertical. Figure 11 shows results for comparison with the top case (100 MHz) in Figure 10, assuming the same manner of survey in terms of antenna orientation, etc. The level spheroidal disc is a stronger scatterer than the vertical projectile, in the sense that the non-normalized value of A_o is substantially greater. At the same time, the value of A_o falls off more steeply as the antenna moves away from the origin. In the region of approximately 45^o polar angle incidence ($Z \sim 0.7$) the disc also produces some ellipticity, but considerably less than the vertical projectile at the same frequency. The disc's patterns are more regular and smooth. Also, the disc backscatter ellipticity is generated by greater prominence of the scattered E_y component, in contrast to the greater E_z component for the vertical projectile. The disc patterns also change much less as a function of frequency (not shown). Thus relative to the vertical projectile, in the level spheroidal disc case these facts taken together indicate 1) a relatively smoother, less geometrically differentiated body, 2) a broader surface facing upwards and smaller lateral cross section, 3) some degree of azimuthally symmetric elongation in the horizontal plane, and 4) less such horizontal elongation than the projectile possesses in the vertical direction.

We expect more dramatic polarization contrasts from a thinner rendition of the disc. Nevertheless, even with its relatively mild lateral elongation the spheroid under consideration shows telltale behavior in a variety of orientations. When its short axis is horizontal and its broad dimension is vertical and aligned with the plane of the transect, survey with the antenna rotated 45^o shows some significant ellipticity generated (Figure 12). However that ellipticity changes little over the Z range where A_o is significant. In other words, polarimetry of the backscatter indicates that the target appears more or less equally elongated vertically from all vantage points over the transect. The relative strength of the E_z

component also reinforces evidence of (x,z) plane elongation over most of the region where A_o is significant. Alternatively, one may keep the antenna in its standard orientation and approach the vertical disc so that its broad side is rotated 45^o about the vertical axis, oblique to the vertical plane containing the transect direction. Figure 13 shows the results at 100 MHz. For antenna locations away from the origin we note negligible ellipticity. This occurs while the incident radiation strikes the broad side of the target to a large extent, tending to generate currents across its broadside and along is its edges. By contrast, when the antenna is moved to a position directly over the oblique target, we note significant depolarization and a degree of ellipticity similar to that observed above, for other cases when the incident field orientation was obliquely transverse to the longer dimension of the disc. These features indicate a target with shape and orientation such that it is generally rounded when seen from the side and elongated, with some rotation within the horizontal plane, when seen from above.

VI. SUMMARY DISCUSSION

The results in this paper suggest ways in which one might use polarimetric GPR to discriminate subsurface metallic shapes, despite ratios of wavelength to target size that have traditionally been viewed as unfavorable for resolution. With the antenna directly over a projectile target, the target length may be inferred from patterns of backscatter magnitude vs frequency. These patterns are also keyed to inclination and rotation of the projectile. Cycles corresponding to higher multiples of half wavelength to target length appear in the pattern when the incident radiation propagates at least to some degree in the direction of the longer dimension of the projectile. This sort of pattern disappears in two limiting orientations: When the long axis of the projectile is in the plane of incidence with E field transverse, in which case the projectile radius may be inferred. When the projectile is completely vertical, polarimetry can reveal that it is vertically elongated and symmetrical about a vertical axis.

Multi-event backscatter magnitude patterns along the survey transect mirror the L/λ frequency effects cited above. They also show distinctive shifts in pattern depending on whether the radiation strikes the projectile nose first or tail first, even with a small ratio of wavelength to geometrical cross section of the target. Future work should focus on the polarimetric content of the successive events along transect records, particularly for arbitrary target orientations. This should provide both orientation and shape data as well as orientation independent information.

Fully polarimetric analysis shows characteristic phenomenology caused principally by the elongated shape of the projectile. Because it has a finite radius, the projectile does not simply depolarize the signal in the manner of a wire or cable. Examination of induced currents and scattered fields both show frequency dependent patterns of depolarization and ellipticity, reflecting an interplay of transverse and longitudinal target dimensions. These effects can help to discriminate the projectile from other axially symmetric shapes. An oblate spheroidal disc is also rotationally symmetry, but about its short axis. From some views it displays an elongated shape, but in a different relation to its axis of symmetry than the projectile. These facts are revealed by polarimetric analysis of backscatter from the spheroidal disc under different angles of attack.

Results to be described in subsequent publications will treat more diverse canonical target shapes; the effects of some details of target morphology, e.g. fins; bistatic observation; and the effect of ground surface proximity on polarimetric signature phenomenology of the sort described above. Signal processing in a field program using a new dual polarized, fully polarimetric, continuously rotatable broadband radar system [23] will incorporate results of the kind shown here as they evolve.

REFERENCES

1. B. Johnson, T.G. Moore, B.J. Blejer, C.F. Lee, T.P. Opar, S. Ayasli, C.A. Primmerman, A Research and Development Strategy for Unexploded Ordnance Sensing, Lincoln Laboratory Project Report EMP-1, Lexington, MA April 1996.

2. C. M. Mackenzie et al, Detecting UXO – putting it all into perspective, SPIE rept 2496, April 1995.

3. C.J. Demos and J.L. Johnson, Martha's Vinyard – An explosive situation: Dune restoration after removal of UXO, Proc. Coastal Zone '89 Conf., p4650 ff.

4. Asbury Park Press, "Artillery Shells under Sandy Hook to be Blown Up," news story Feb 4, 1998.

5. H. Nelson, ESTCP Ongoing Project Review 1998, citing figures from the US Army Corps of Engineers Huntsville Center.

6. Scitek, Inc, Study on the Feasibility of Mass Area Ordnance Decontamination, Report TR-161, for Naval EOD Facility, AD-A007 610, 1974.

7. K. O'Neill, R.F. Lussky, and K.D. Paulsen, Scattering from a metallic object embedded near the randomly rough surface of a lossy dielectric, IEEE Trans.Geosci. Remote Sensing, vol 34, 367-376, 1996.

8. K. O'Neill, Exploration of innovative radar sensing schemes for subsurface object detection, Proc. IGARSS'97, 1135-1137, 1997.

9. K. O'Neill, Radar detection of near-surface buried metallic reflectors in wet soil, Proc. IGARSS'97, 1288-1290, 1997.

10. K. O'Neill, Radar sensing of surface layers and near surface objects, accepted for publication, IEEE Trans. Geosci. Remote Sensing, 1998.

11. K. O'Neill (1999). Broadband bistatic coherent and incoherent detection of buried objects beneath randomly rough surfaces, accepted for publication, IEEE Trans. Geosci. Rem. Sens., 1999

12. H. Brunzell, Detection of shallowly buried objects using impulse radar, IEEE Trans. Geosci. Rem. Sens., vol 37(2),II, 875-886, 1999.

13. A. J. Witten, J.E. Molyneux, and J.E. Nyquist, Ground penetrating radar tomography: Algorithms and case studies, IEEE Trans. Geosci. Remote Sens., vol 32, 461-467, 1994.

14. G. Zhang, and L. Tsang, Application of angular correlation function of clutter scattering and correlation imaging in the target detection, IEEE Trans. Geosci. Remote Sens., vol.36(5), 1485-1493,1998.

15. S.A. Haider, K. O'Neill, and K.D. Paulsen, Influence of ground surface proximity on polarimetric properties of radar scattering from buried metallic objects, in prep.

16. J-A Kong, *Electromagnetic Wave Theory*, New York: Wiley, 1990.

17. J.E. Akin, *Finite Elements for Analysis and Design*, New York: Academic Press, 1994.

18. S.A. Arcone, K. O'Neill, A.J. Delaney, and P.V. Sellmann, UXO Detection at Jefferson proving Ground using Ground-Penetrating Radar, CRREL Report CR670, in editing, 1999.

19. F.T. Ulaby and C. Elachi (eds), *Radar Polarimetry for Geoscience Applications*, Norwood MA: Artech House, Inc, 1990, ch. 1.

20. M. Born and E. Wolf, *Principles of Optics*, New York: Pergamon Press, 1965, ch. 1.

21. N. Geng, C.E. Baum, and L. Carin, On the low frequency natural response of conducting and permeable targets, IEEE Trans. Geosci. Remote Sens., vol 37(1), II, 347-359, 1999.

22. J.J. Bowman, T.B.A. Senior, and P.L.E. Uslenghi, (eds), *Electromagnetic and Acoustic Scattering by Simple Shapes*, New York: Elsevier, 1988.

23. C.C. Chen, A new ground penetrating radar antenna design: The horn-fed Bowtie (HFB), Proc. AMTA97 Symp. 67-74, 1997.

FIGURE CAPTIONS

FIGURE 1. The setup, showing projectile and antenna in reference configurations.

FIGURE 2. Far field patterns for antenna 0.4 m by 0.8 m, with smoothing of current distribution across narrow (z) dimension. 300 MHz, $\kappa = 10.4 + 0.5i$.

FIGURE 3. Normalized scattered electric field above projectile oriented in the Y direction.

FIGURE 4. Normalized scattered E field above target for various projectile inclinations and rotations θ_d, θ_x.

FIGURE 5. Normalized scattered E field when projectile axis is in (x,z) plane, from different vantage points Z_a.

FIGURE 6. Backscattered E_z field magnitudes along transect, at various frequencies, when the projectile is inclined at 45 degrees with nose up ($\theta_d = 225^o$, $\theta_x = 0$) and the antenna is rotated $\theta_a = 45^o$.

FIGURE 7. Backscattered E_z field magnitudes along transect, at various frequencies, when the projectile is inclined at 45 degrees with nose down ($\theta_d = 45^o$, $\theta_x = 0$) and the antenna is rotated $\theta_a = 45^o$.

FIGURE 8. Backscatter polarization ellipses for three antenna locations (top) and corresponding continuous polarimetric parameter distributions along the transect (bottom) for scattering from a 25 cm radius sphere surrounded by soil, at 50 MHz and 250 MHz.

FIGURE 9. Backscatter polarization ellipses vs frequency for projectile rotated horizontally ($\theta_d = 0$, $\theta_x = 45^o$).

FIGURE 10. Backscattered E field component magnitudes (left) and corresponding polarization parameters (right) for vertical projectile, nose down, at three different frequencies, when antenna is rotated so $\theta_a = 45^o$ everywhere along the transect.

FIGURE 11. Backscatter characteristics at 100 MHz from level spheroidal disc, when the antenna is rotated so $\theta_a = 45^o$ everywhere along the transect.

FIGURE 12. Backscatter characteristics at 100 MHz from disc vertical in the (x,z) plane, with antenna rotated so $\theta_a = 45^o$ everywhere along the transect

FIGURE 13. Backscatter characteristics at 100 MHz from vertical disc rotated 45^o relative to the (x,z) plane, with antenna in standard orientation.

ACKNOWLEDGMENT

This work and its publication were supported by the United States Army's BT25 Program (Installation Restoration); and by the United States Department of Defense's Environmental Security Testing and Certification Program.

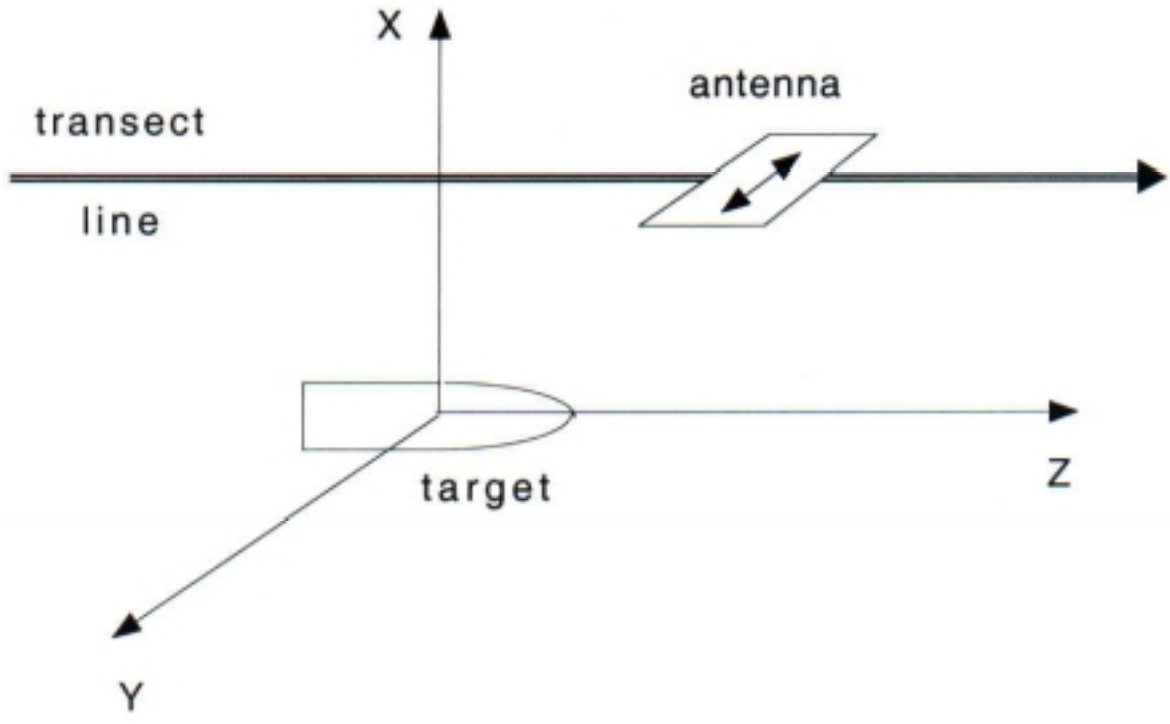

FIGURE 1

Far field patterns for antenna 0.4 by 0.8 m,
with smoothing of currents distributions across the short (Z) direction
300 MHz, κ = 10.4

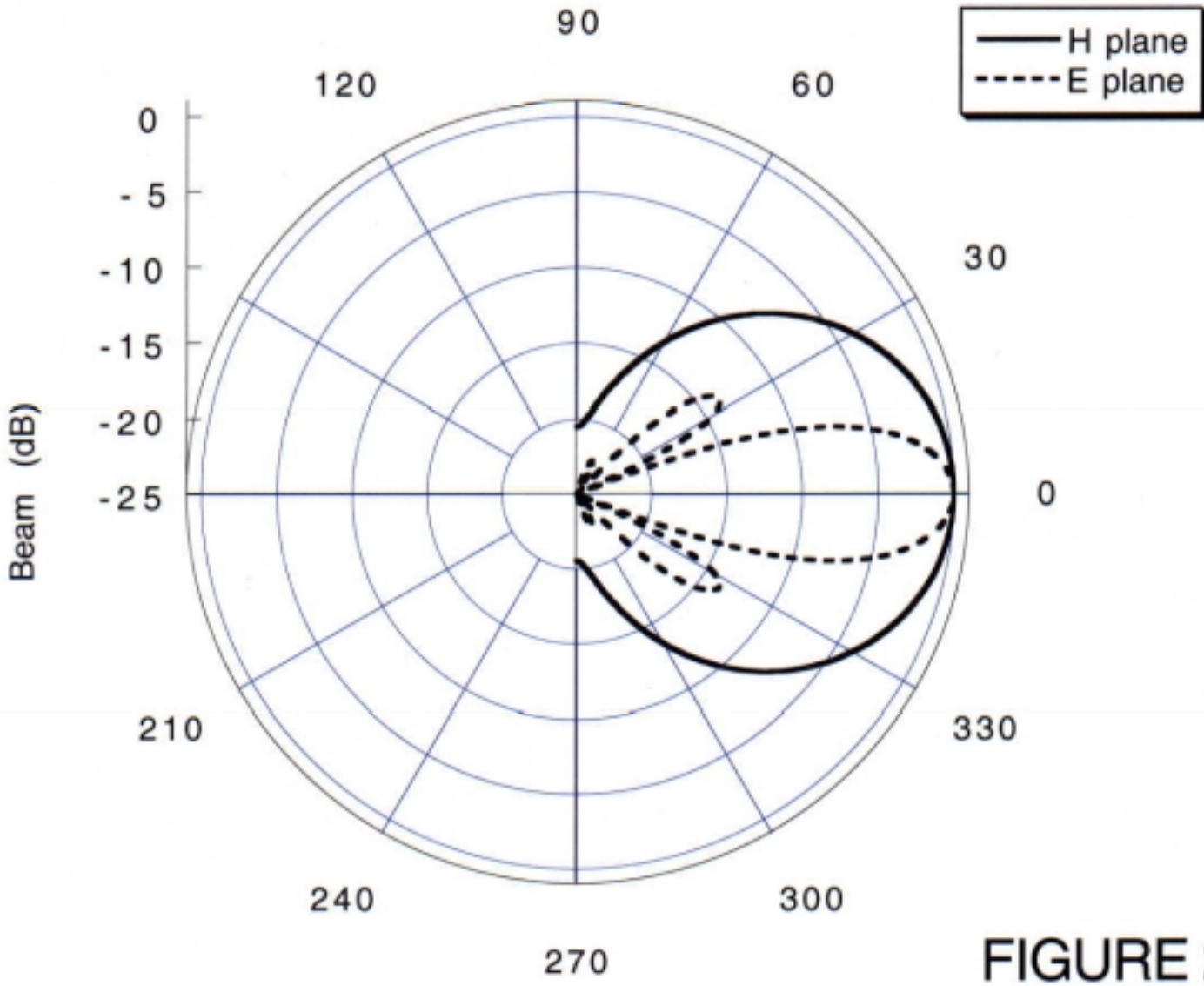

FIGURE 2

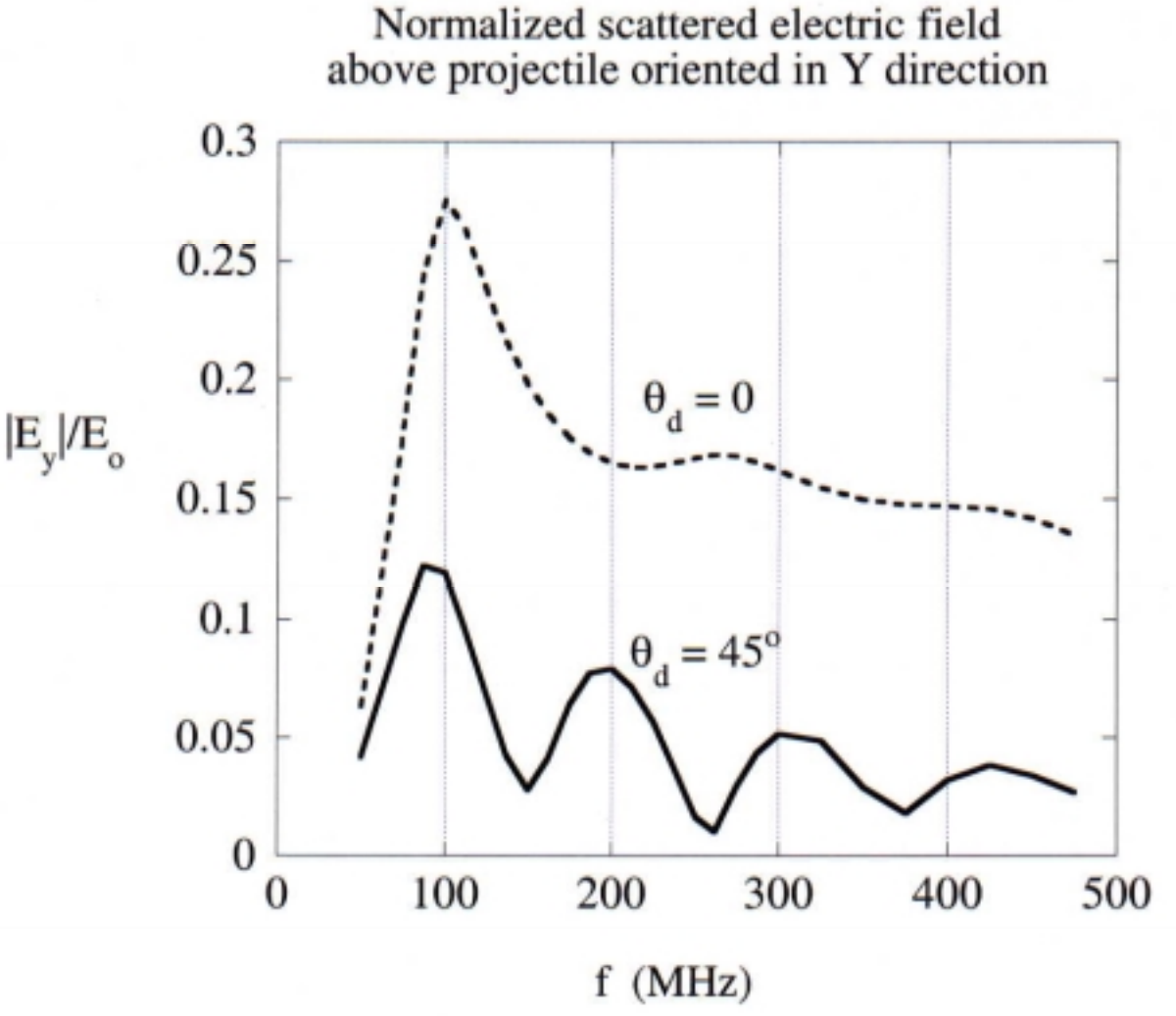
Normalized scattered electric field
above projectile oriented in Y direction
|E_y|/E_o
0.3
0.25
0.2
0.15
0.1
0.05
0
θ_d = 0
θ_d = 45°
0
100
200
300
400
500
f (MHz)

FIGURE 3.

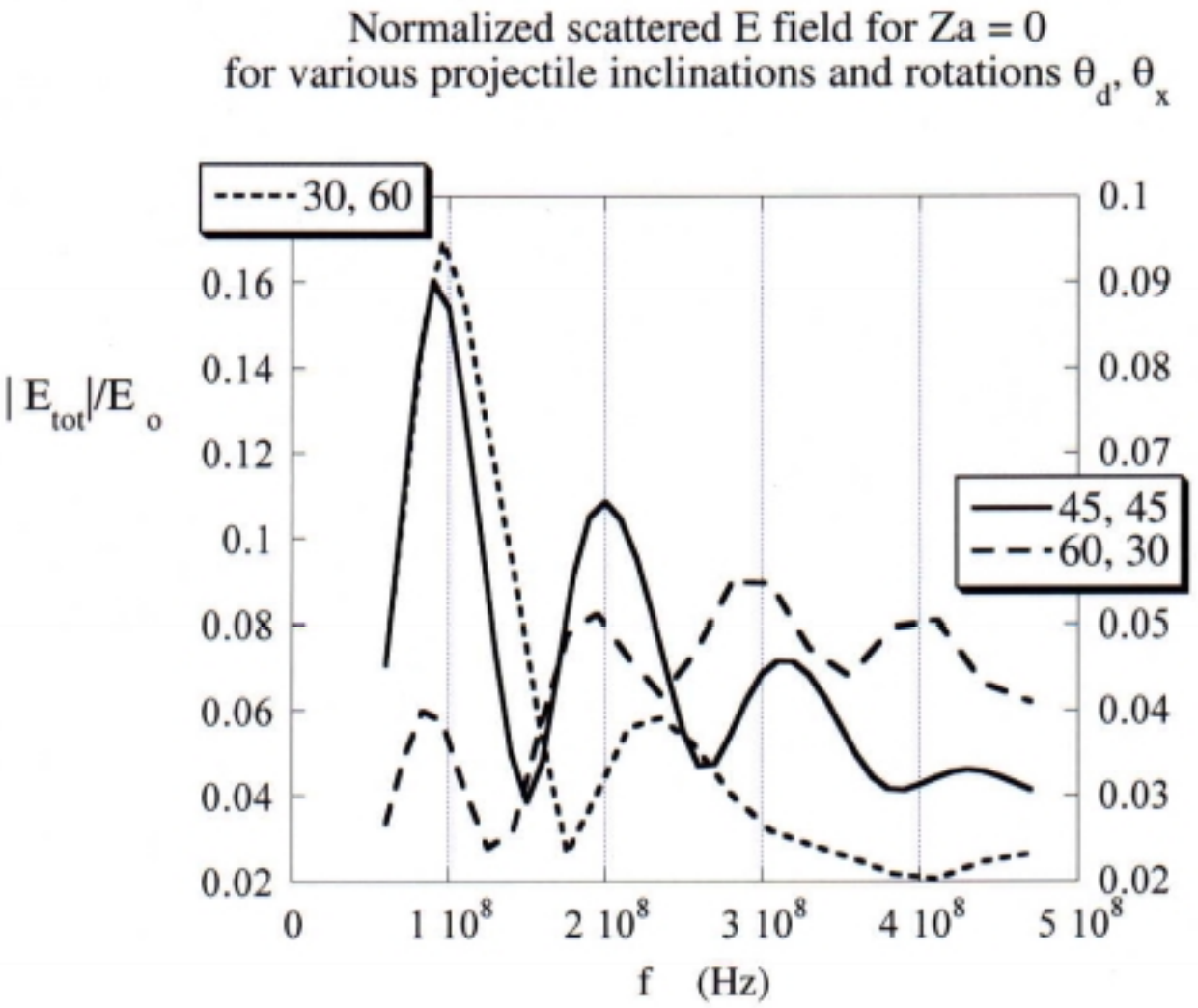
Normalized scattered E field for Za = 0
for various projectile inclinations and rotations θd, θx
-----30, 60
——45, 45
– – -60, 30
| E tot |/E o
0.16
0.14
0.12
0.1
0.08
0.06
0.04
0.02
0.1
0.09
0.08
0.07
0.05
0.04
0.03
0.02
0
1 10^8
2 10^8
3 10^8
4 10^8
5 10^8
f (Hz)

FIGURE 4.

Normalized scattered E field when projectile axis
is in (x,z) plane, from different vantage points in Z_a

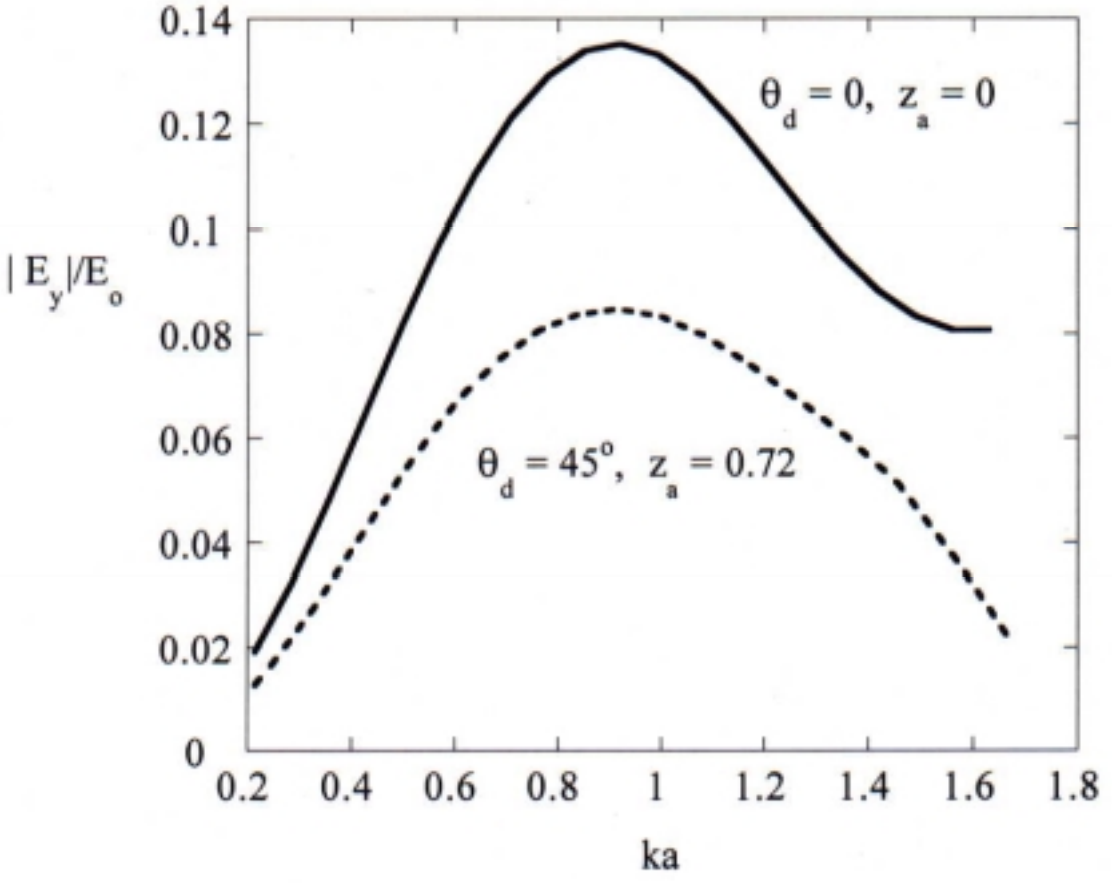

Figure 5

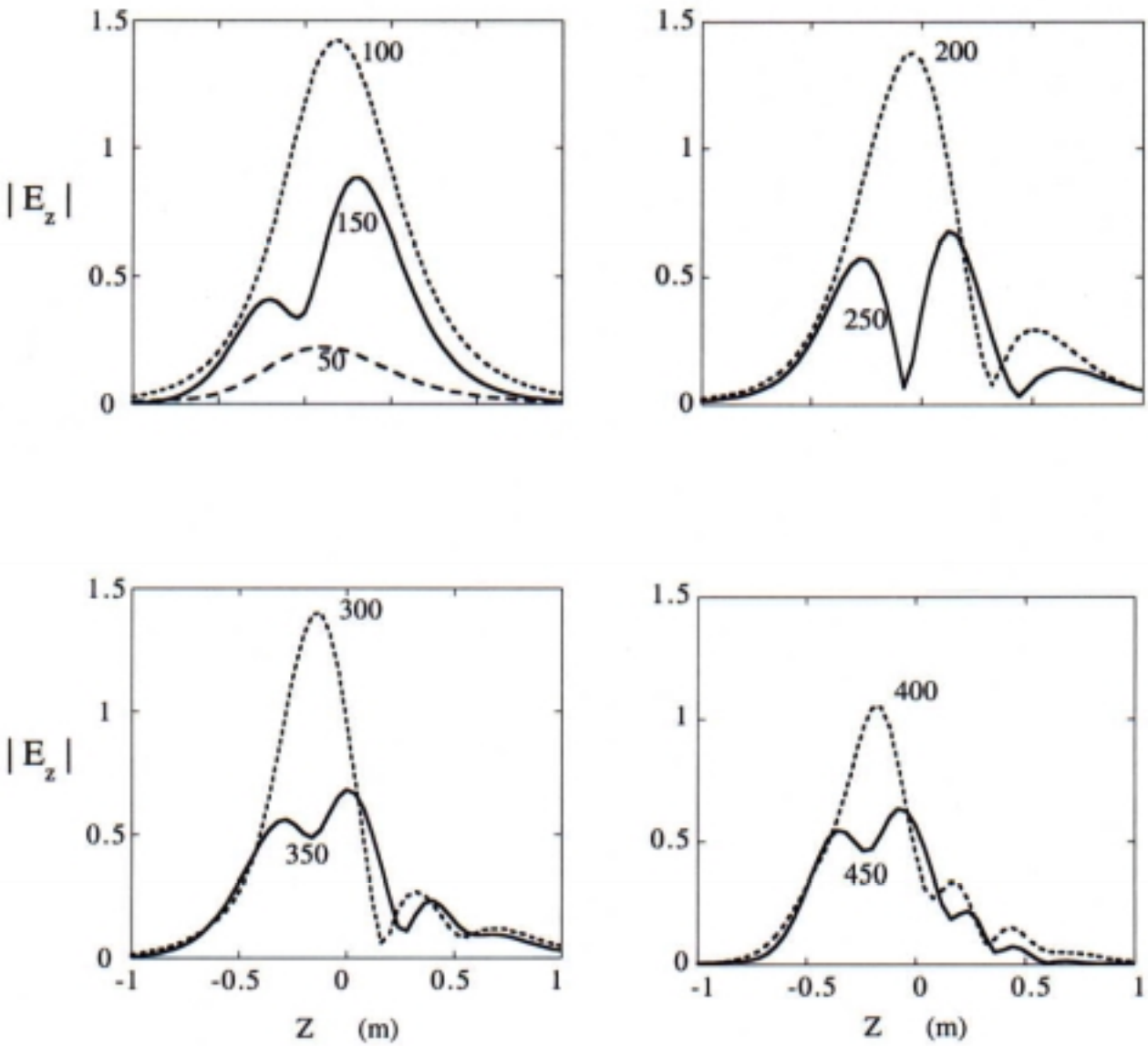

FIGURE 7

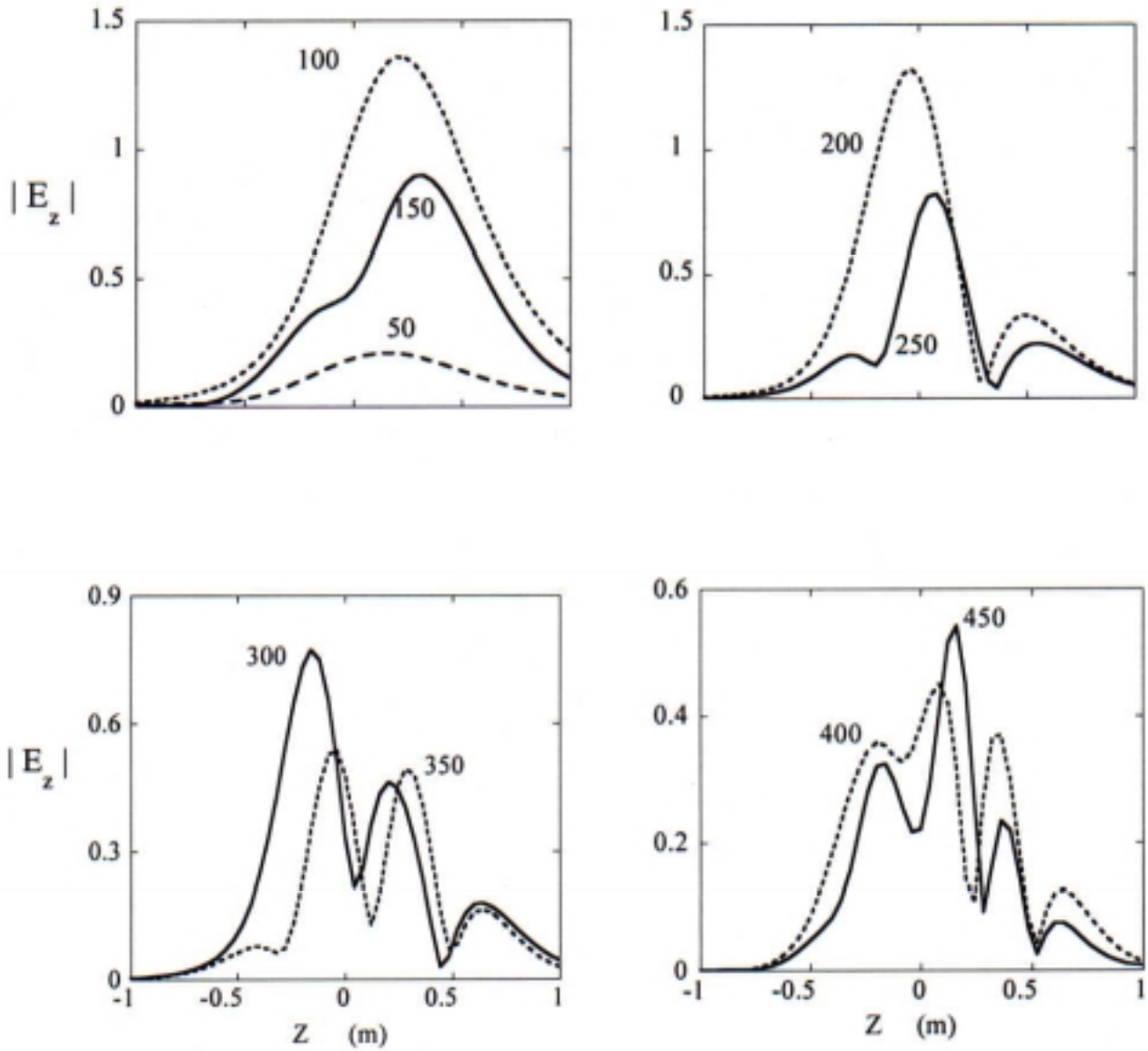
1.5
1
0.5
0
| E_z |
100
150
50
200
250
0.9
0.6
0.3
300
350
0.6
0.4
0.2
450
400
-1
-0.5
0
0.5
1
Z (m)

FIGURE 6

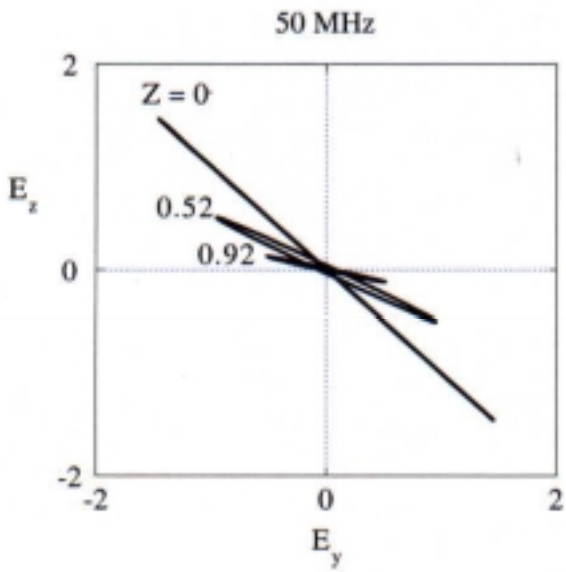
50 MHz
Z = 0
0.52
0.92
E_z
E_y
2
0
-2
-2
0
2

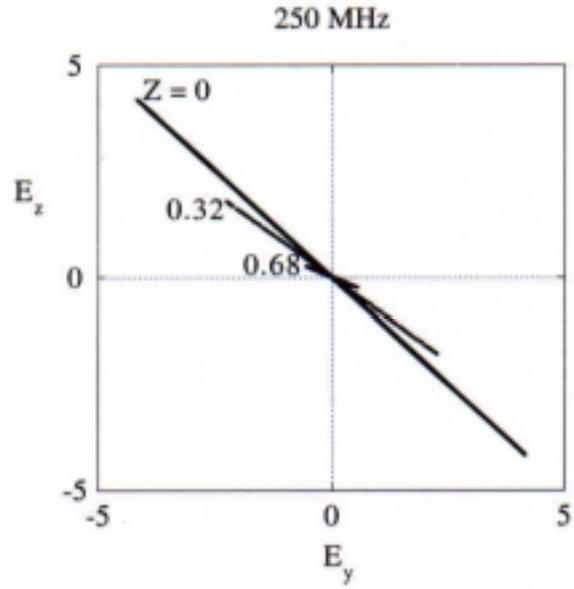
250 MHz
Z = 0
0.32
0.68
E_z
E_y
5
0
-5
-5
0
5

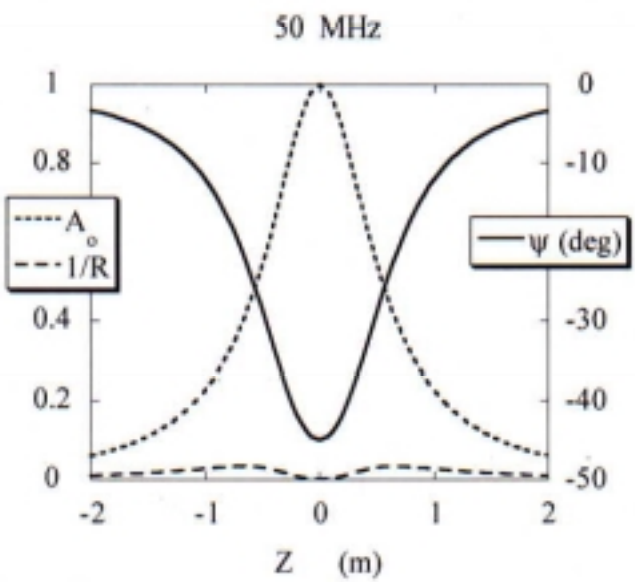
50 MHz
A_o
1/R
ψ (deg)
Z (m)
1
0.8
0.4
0.2
0
-10
-30
-40
-50
-2
-1
0
1
2

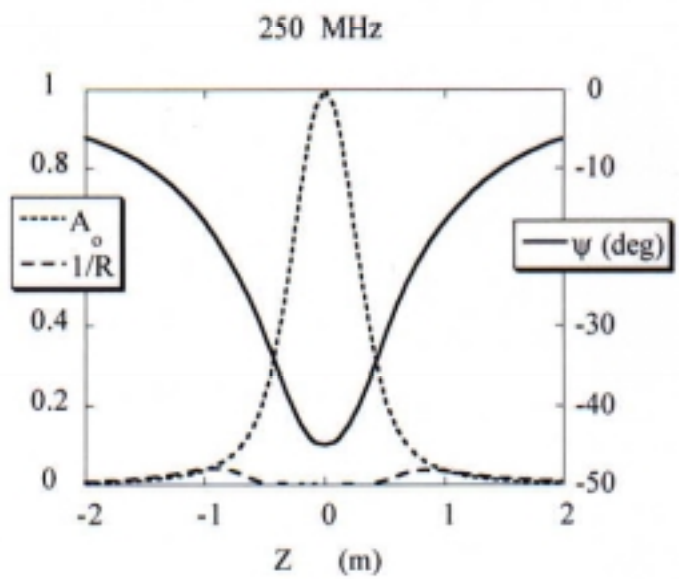
250 MHz
A_o
1/R
ψ (deg)
Z (m)
1
0.8
0.4
0.2
0
-10
-30
-40
-50
-2
-1
0
1
2

FIGURE 8

Polarization ellipses vs frequency for
projectile rotated horizontally 45°

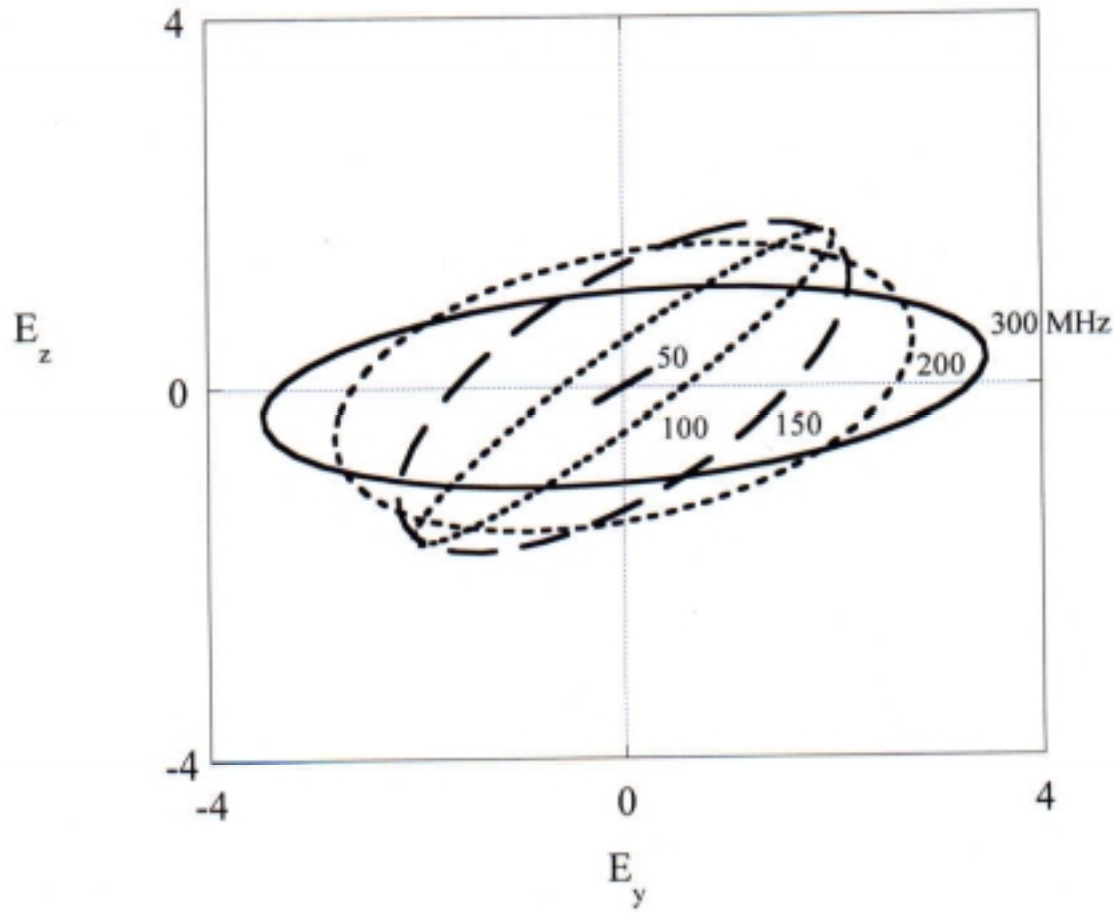

FIGURE 9

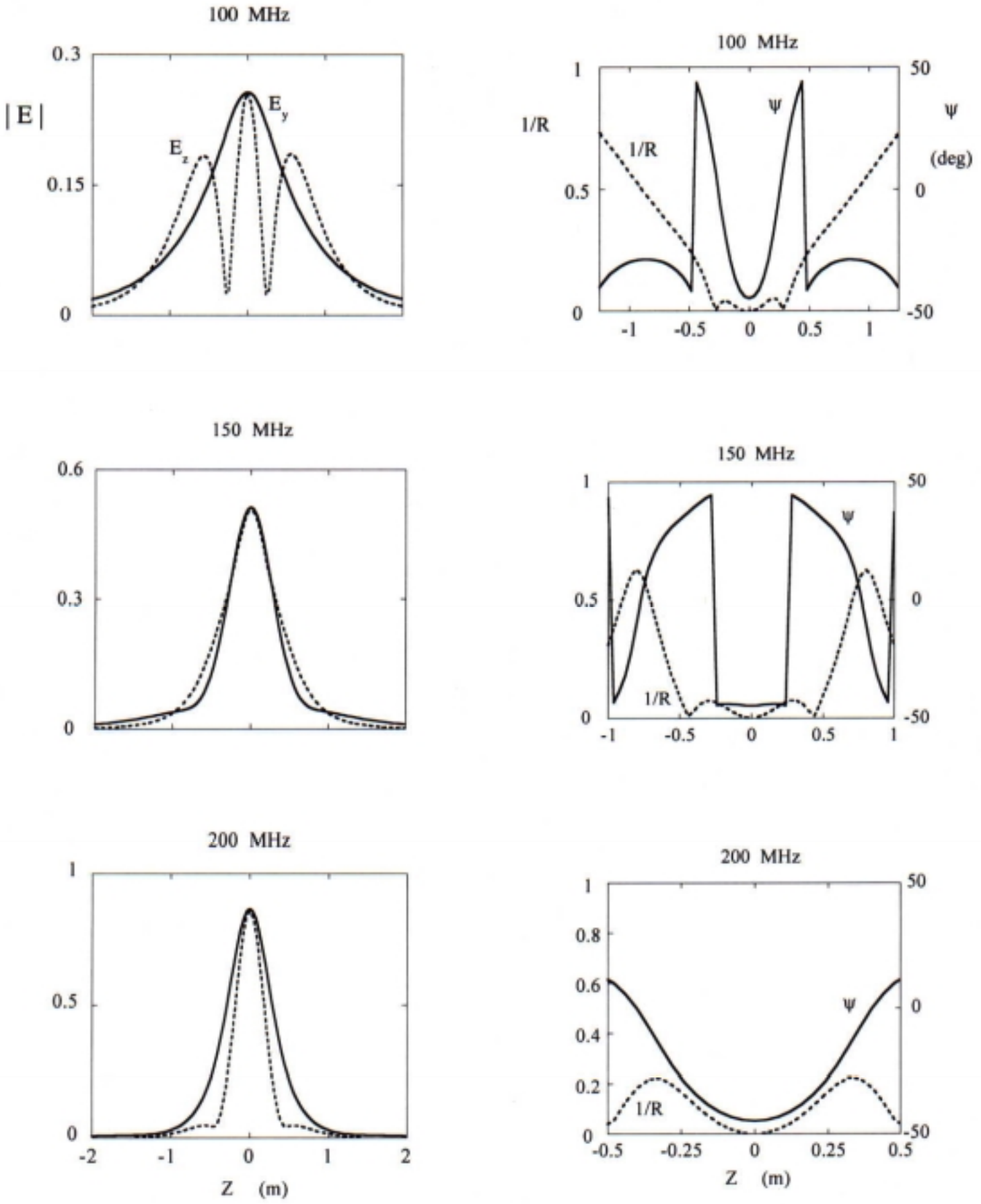
100 MHz
|E|
E_y
E_z
100 MHz
1/R
ψ
(deg)
150 MHz
150 MHz
200 MHz
200 MHz
Z (m)
Z (m)

Figure 10.

Backscatter from level spheroidal disc at 100 MHz
illuminated by antenna with 45° rotation

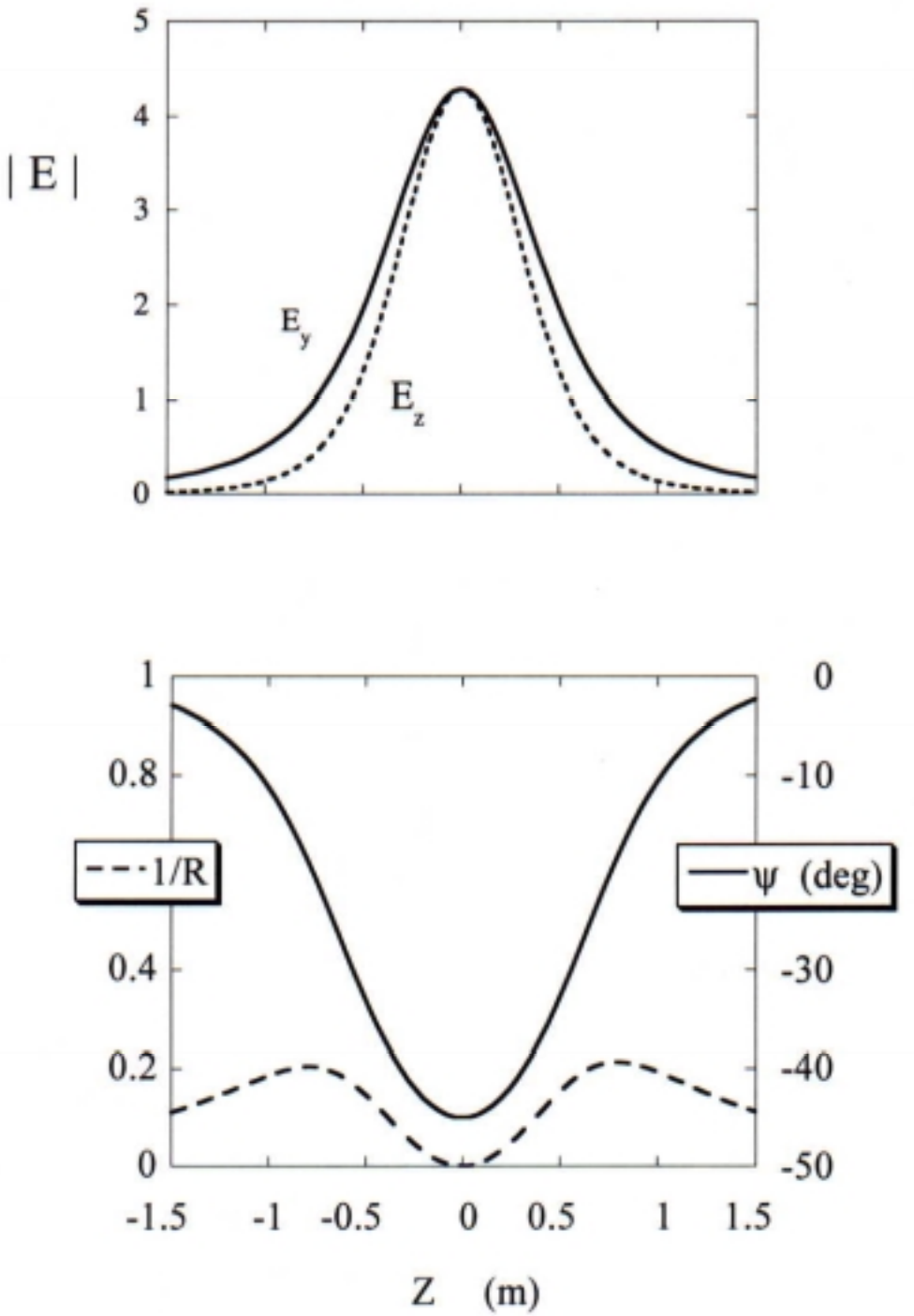

FIGURE 11.

Backscatter from disc vertical in (x,z) plane
with antenna rotated θ_a => 45°, 100 MHz

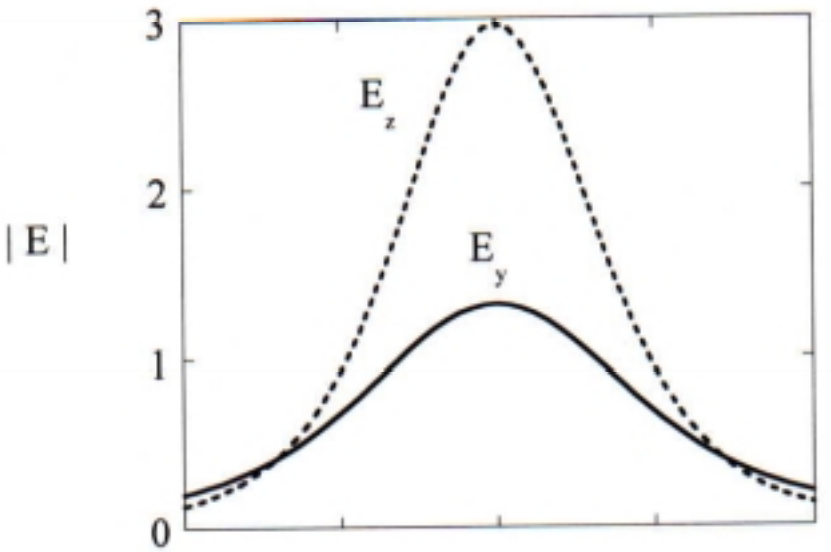

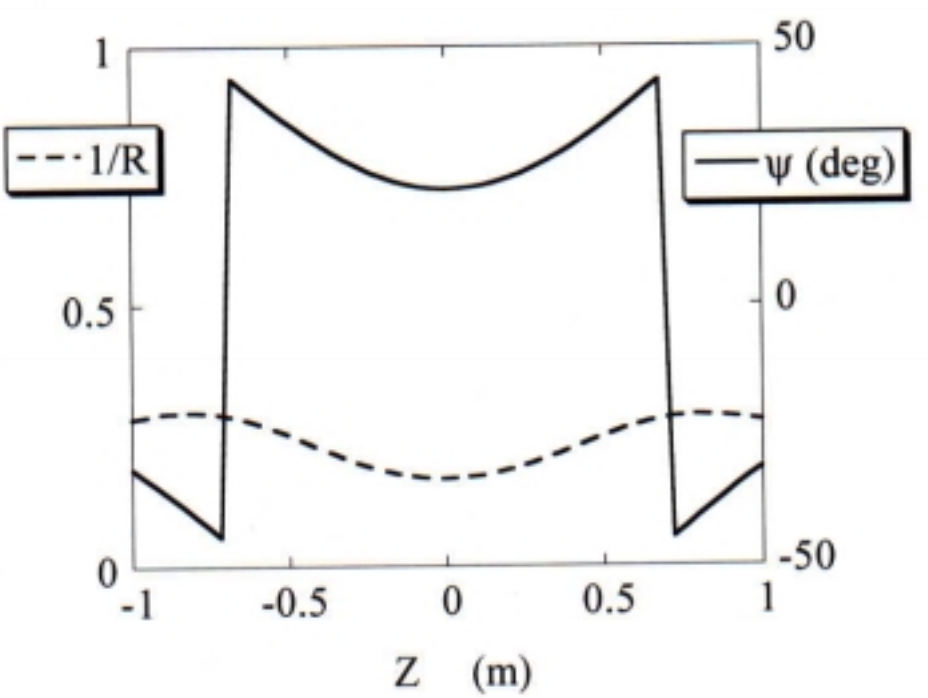

FIGURE 12.

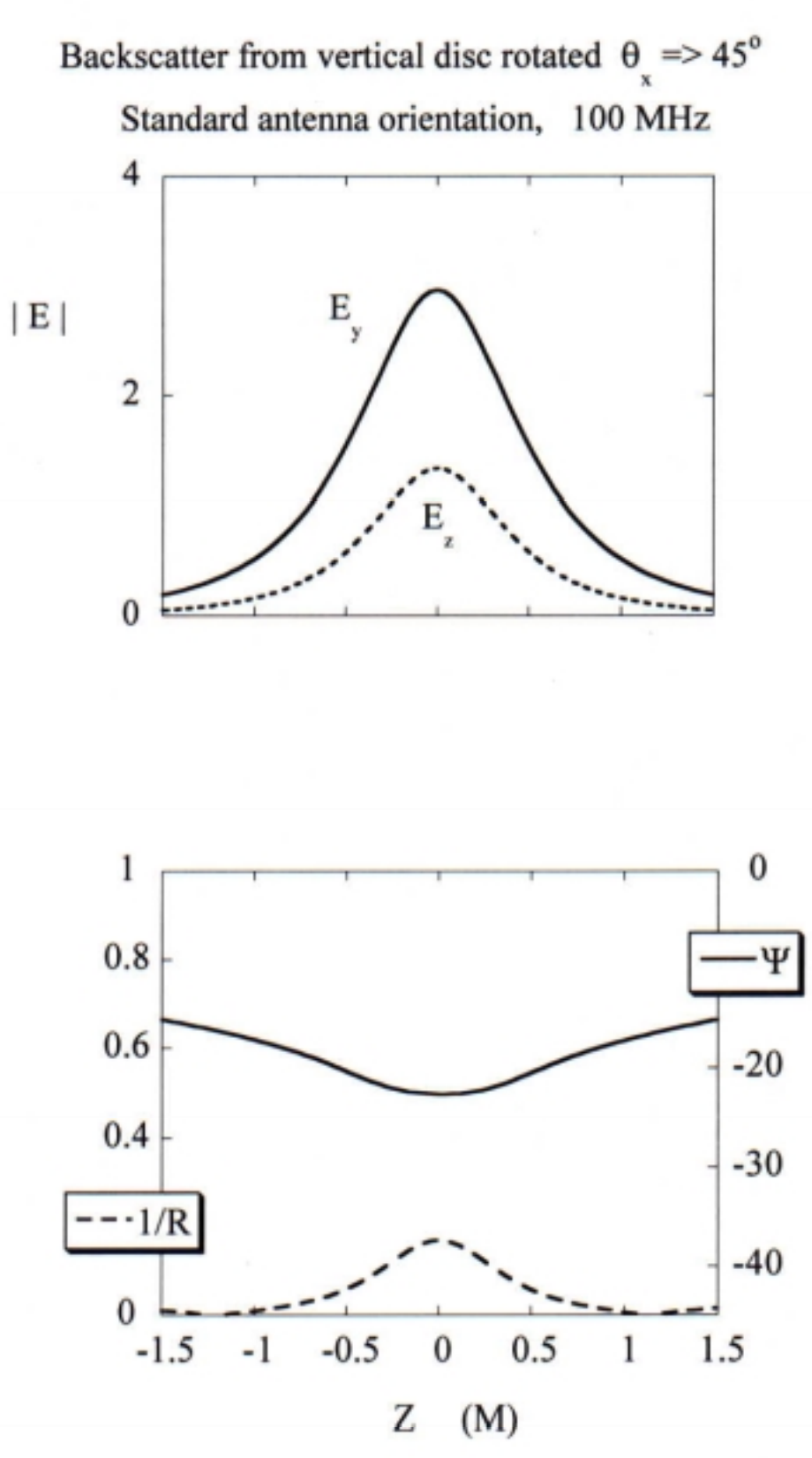
Backscatter from vertical disc rotated θx => 45°
Standard antenna orientation, 100 MHz
|E|
4
2
0
Ey
Ez
1
0.8
0.6
0.4
0
Ψ
1/R
0
-20
-30
-40
-1.5
-1
-0.5
0
0.5
1
1.5
Z (M)

FIGURE 13.